

Spatiotemporally resolved measurements of electric field around a piezoelectric transformer using electric-field induced second harmonic (E-FISH) generation

Jinyu Yang¹ , Edward V Barnat^{2,*}, Seong-kyun Im^{1,3}  and David B Go^{1,4,*} 

¹ Department of Aerospace and Mechanical Engineering, University of Notre Dame, Notre Dame, IN 46556, United States of America

² Sandia National Laboratories, Albuquerque, NM 87185, United States of America

³ School of Mechanical Engineering, Korea University, Seoul 02841, Republic of Korea

⁴ Department of Chemical and Biomolecular Engineering, University of Notre Dame, Notre Dame, IN 46556, United States of America

E-mail: evbarna@sandia.gov and dgo@nd.edu

Received 21 September 2021, revised 15 November 2021

Accepted for publication 6 December 2021

Published 7 March 2022



CrossMark

Abstract

When a piezoelectric transformer (PT) is actuated at its second harmonic frequency by a low input voltage, the generated electric field at the distal end can be sufficient to breakdown the surrounding gas, making them attractive power sources for non-equilibrium plasma generation. Understanding the potential and electric field produced in the surrounding medium by the PT is important for effectively designing and using PT plasma devices. In this work, the spatiotemporally resolved characteristics of the electric field generated by a PT operating in open air have been investigated using the femtosecond electric field-induced second harmonic generation (E-FISH) method. Electric field components were determined by simultaneously conducting E-FISH measurements with the incident laser polarized in two orthogonal directions relative to the PT crystal. Results of this work demonstrate the spatial distribution of electric field around the PT's output distal end and how it evolves as a function of time. Notably, the strongest electric field appears on the face of the PT's distal surface, near the top and bottom edges and decreases by approximately 70% over 3 mm. The time delay between the PT's input voltage and measured electric field indicates that there is an about 0.45π phase difference between the PT's input voltage and output signal.

Keywords: piezoelectric transformer, second harmonic generation, electric field, surface potential, COMSOL multiphysics

(Some figures may appear in color only in the online journal)

* Authors to whom any correspondence should be addressed.

1. Introduction

The piezoelectric effect of non-centrosymmetric crystals, such as lead zirconate titanate ($\text{Pb}[\text{Zr}_x\text{Ti}_{(1-x)}]\text{O}_3$ ($0 \leq x \leq 1$), PZT) and lithium niobate (LiNbO_3 , LN), offer the opportunity to develop energy conversion plasma sources that do not rely on a high-voltage power supply [1]. When a piezoelectric crystal undergoes mechanical deformation, a strong polarization can be induced (called the direct piezoelectric effect), leading to very high surface fields that in turn breakdown the surrounding gas and form a plasma. This principle is behind various commercial spark generation devices such as gas grill igniters [2], and the characteristics of the produced plasmas are analogous to transient sparks [3–5]. Limited by insufficient knowledge about mechanical-to-plasma energy conversion and its manipulation, there is, to our knowledge, no published report on using the direct piezoelectric effect to form low-temperature atmospheric pressure plasmas. Alternatively, piezoelectrics are most often utilized for nonequilibrium low-temperature plasma generation in the form of piezoelectric transformers (PTs).

Classic PTs are compact, solid state, high-power density electrical transformers that can amplify a low-voltage alternative current (AC) input to orders-of-magnitude gains through intrinsic electromechanical resonance [6]. Due to the limited performance of available materials, early PT concepts were not useful until the profound invention of Rosen [7]. Subsequently, Rosen-type PTs were initially used as replacements for electromagnetic transformers [6] and then widely utilized as low power (usually in the range of 1–10 W), step-up voltage converters for cold cathode fluorescent lamp (CCFL) backlighting [8–10]. Research conducted during this period was mainly concerned on modifications of Rosen's prototype, involving mounting or housing strategies, driving circuitry, novel materials, and fabrication technologies [6].

While classic Rosen type PTs are less favorable for recent applications that require high power conversions (on the order of 10^1 – 10^2 W) [6], their ability to generate very high voltage outputs, in addition to their small size and weight, has made them very attractive as plasma sources, what is often referred to as a piezoelectric direct discharge plasma [11–13]. First demonstrated by Itoh *et al* [14], this novel approach to plasma generation has been demonstrated for a variety of modes of gas discharges operating in different gases and over a wide range of pressures (10^{-3} – 10^3 Torr) [11, 14–20]. Depending on the configuration, PTs either work as the high voltage source, biasing a metal electrode [1, 21–24], or directly as a plasma electrode, where the plasma forms directly off the PT surface [1, 12, 13, 25]. Research on PTs for plasma generation has focused on providing a comprehensive understanding about PT-driven plasma generation, including the principle of operation [13, 26], modifications of the original rectangular, single layer PT configuration [22], electrical and optical properties [23, 25, 27], numerical modeling [28–31], and characterizations of possible applications [11–13, 18, 32–36].

One key parameter of interest is the electric field surrounding the PT's distal end where the high surface voltage is induced. Whereas in conventional plasma sources, high

voltage probes or surface voltmeters can be employed to measure the applied voltage on the electrode and thus deduce the consequent electric field, in PT-driven plasma generation these tools cannot be utilized because they inevitably interfere with the PT's vibration [37] and/or lead to changes in the PT's output load and surrounding environment [26, 38]. Based on the relative probe method [39, 40], Teranishi *et al* first proposed a non-contact approach for absolute surface potential measurement on a PT device [37, 41]. Measurements using this approach, along with its modifications, have been compared to analytical models developed by Pigache and collaborators [31, 38]. Despite the measured potential values showing satisfactory agreement with the analytical predictions in some areas on the PT's surface [38, 42], discrepancies suggest that it would be impactful to have a secondary experimental tool for comparison, validation, and an overall deeper understanding of the underlying physics.

Electric field measurements, on the other hand, are considerably more challenging, and there is a lack of experimental data on how the electric field distributes around the PT and varies with time [30]. Methods such as capacitive probes [43–45], electrostatic fluxmeters [46], and electro-optic probes based on Pockels effect [47–50] are not optimal because they inevitably disturb the electric field distribution. While optical emission spectroscopy based on the application of polarization-dependent Stark splitting and shifting can leave the field undisturbed [51–53], the emission-based method is only sensitive to specific species (e.g. hydrogen and helium), has a relatively low temporal resolution especially for PT-driven discharges, and cannot be applied to conditions where no or few photons are emitted (e.g. prior to breakdown or regions outside the discharge area). To that end, a nonintrusive method that is not constrained by the above factors would be useful for understanding the behavior of PT devices.

In recent years, electric field-induced second harmonic generation (E-FISH) has been utilized over a wide spectrum of non-equilibrium plasma research, spanning electric field measurements in corona discharges [54, 55], surface dielectric barrier discharges [56, 57] and plasma jets [58], to studies of ionization waves [59–61]. Its straightforward, nonintrusive, and species-independent nature [62], as well as high measurement resolution in space (sub-mm) and time (sub-ns), makes E-FISH a promising technique that can be applied to investigate the electric field distribution around a PT.

The objective of the present work is to directly measure the electric field distributed around the output distal end of a rectangular, single-layer Rosen type PT plasma source using the E-FISH technique. Spatially and temporally resolved E-FISH measurements were conducted at or near the PT surface under conditions that are slightly below the breakdown threshold and just above the breakdown threshold. We found that there was typically a dominant electric field component at each surface, evolving periodically in time. A comparison of the measured electric field and input voltage shows that the PT's output is phase-shifted from its input. Measurements of the electric field during plasma generation proved to be more challenging due to the relatively low plasma density, effects of the plasma on the PT's operation, and the stochastic nature of

plasma formation off the surface of the PT [25], but the data show that the electric field was slightly lower after breakdown, likely due to a decrease in the voltage gain of the PT when the plasma is active.

2. Experimental method

2.1. PT and its operation

In this work, a 53 mm long \times 7.5 mm wide \times 2.6 mm thick commercially available cuboid-shaped Rosen type PZT PT (Steiner & Martins, INC. model SMSTF68P10S9) was utilized. As shown in figure 1, this PT has a primary part that is polarized transversely to the vibration, whereas its secondary part is polarized longitudinally to the vibration. When biasing the primary part of the PT with a low-voltage (on the order of 10 V) AC power supply, the converse piezoelectric effect induces vibrations in the PT that subsequently applies mechanical stress to the adjacent secondary part, which in turn forms a high-voltage AC output at the distal end due to the direct piezoelectric effect. Analogous to electromagnetic coupling in a conventional magnetic core transformer, this process in PT is called electromechanical coupling. The performance of a Rosentype PT can be characterized by the voltage gain or voltage transformation ratio, which can be evaluated by:

$$\frac{V_{out}}{V_{in}} \propto k_t k_l Q n \frac{L}{H}, \quad (1)$$

where V_{in} is the input to the primary part, V_{out} is the output at the distal end of the secondary part, k_t are k_l are transverse and longitudinal piezoelectric coupling coefficients respectively [63], Q is the mechanical quality factor, n is the number of layers, which is $n = 1$ for the single-layer PT used here, and L and H are the PT's total length and thickness.

Piezoelectric resonance of the PT can occur at multiple frequencies [12], and the most efficient electrical-mechanical-electrical energy conversion occurs when the PT is excited in the vicinity of harmonics of its resonant frequency (piezoelectric resonance), with possible voltage gains on the order of 10^1 – 10^3 [1, 23, 32]. The lowest frequency that has been widely used for voltage transformation is the second harmonic (usually in the range of 50–150 kHz). The PT operating at its second harmonic has nodal points of minimal displacement at $1/4$ and $3/4$ of the total length, indicated by the black dashed lines in figure 1. In this work, the PT was mounted on an apparatus that pinned the PT at those nodes such that minimum damping of the vibration can be achieved. At the $L/4$ node, plastic, rather than metal, mounts were employed to avoid unfavorable gas breakdown due to triple junction enhancement [64]. For the same reason, the native silver electrode coated on the PT's output distal end was etched away using concentrated nitric acid ($\sim 70\%$) because the as-purchased PT is originally designed to be a high-voltage power source.

To actuate the PT, a sinusoidal signal from a function generator (SRS DS345) was amplified by an RF amplifier (Krohne-Hite Corporation, Model 7620) to the desired voltage amplitude ($12.5 V_a$ for the study below breakdown threshold and

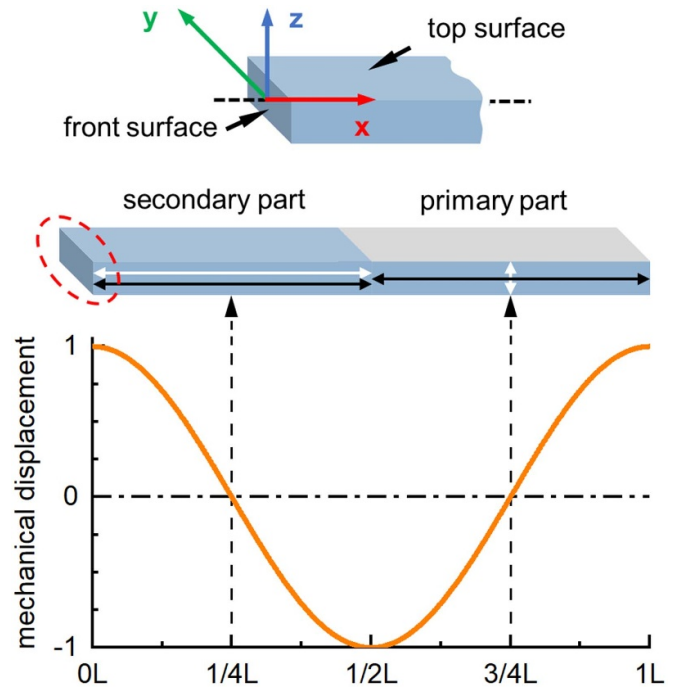


Figure 1. Schematic of a rectangular, single-layer Rosen-type PZT PT utilized for this work. The gray areas on the top and bottom (hidden) on the primary part represent the input electrodes. White arrows indicate the polarization directions, and black arrows indicate the mechanical stress. The output distal end circled by the red dashed line, is zoomed and shown above. The bottom plot illustrates the mechanical displacement wave formed when running the PT at its second harmonic.

$14.4 V_a$ for the study above breakdown threshold) and then applied to the faces of the primary part (gray areas in figure 1). Input current was measured with a Rogowski coil current sensor (Pearson Electronics, Model 2877). Both input voltage and current were simultaneously monitored using a digital oscilloscope (Lecroy, Model HDO4140a) at a sampling rate of 125 MHz. The resonant frequency (67.262 kHz for this PT) was determined by monitoring when the input current was in phase with the input voltage [25].

2.2. E-FISH

E-FISH is a 3rd order nonlinear optical process that arises from interactions between electric fields of an external source and a probe laser. Usually, second harmonic generation (SHG) is impossible in a centrosymmetric system. However, this symmetry can be destroyed by the presence of an external electric field, resulting in the molecules radiating light at the second harmonic frequency [61]. This process can be described by the following expression:

$$P_i^{(2\omega)} = \frac{3}{2} N \chi_{ij,k,l}^{(3)}(-2\omega, 0, \omega, \omega) E_j^{(ext.)} E_k^{(\omega)} E_l^{(\omega)}, \quad (2)$$

where $P_i^{(2\omega)}$ is the induced light's polarization at 2ω , N is the number density of the gas, $\chi_{ij,k,l}^{(3)}(-2\omega, 0, \omega, \omega)$ is the 3rd order nonlinear susceptibility tensor, which is a function

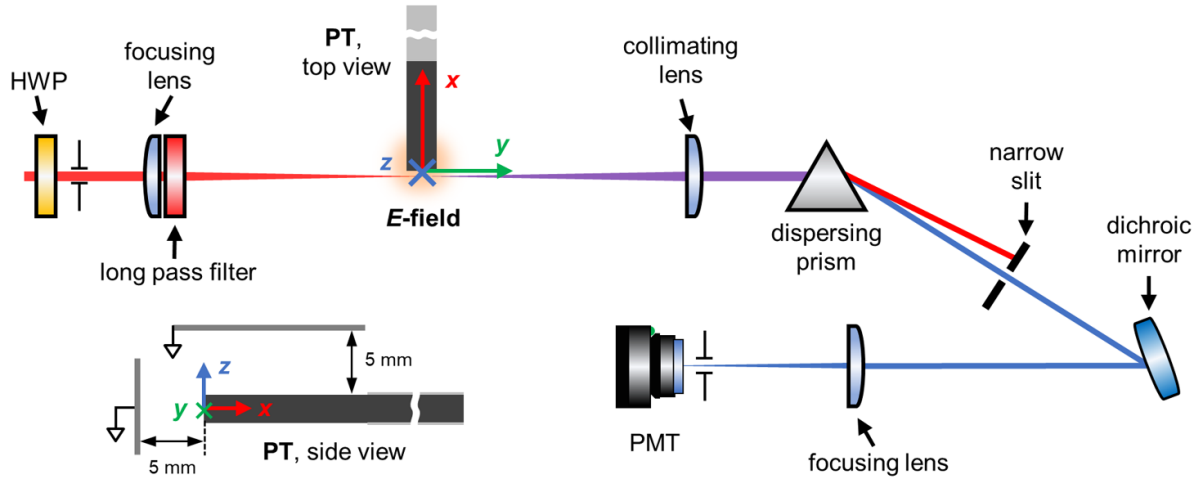


Figure 2. Simplified schematic of the experimental apparatus utilized in the femtosecond E-FISH system for this study. An HWP was employed to regulate the pump beam's polarization. The pump beam passed through a long pass filter before focusing on the region of study. The residual pump beam was blocked by a narrow slit, whereas the SHG beam was reflected by a dichroic mirror and then focused on to the entrance of the PMT. The sketch in the lower left portion shows the grounded plate configuration utilized for the electrical potential distribution measurements. The coordinate system used in this work has the x axis along the PT's longitudinal direction, y axis along the laser beam propagation, and z axis along the PT's transverse direction. Adopted from [61].

of field orientation and molecular dipole moments [65], and $E_j^{(\text{ext.})}$ is the external electric field, while $E_k^{(\omega)}$ and $E_l^{(\omega)}$ are electric fields of incident laser(s), which can be treated to be equal when only a single laser source is utilized. The subscripts denote the polarizations of the respective fields. Rather than electric field measurements, the initial work with this technology was to determine the nonlinear susceptibility (also called hyperpolarizability) of different gases, in which a known electric field was given [65–68]. Recently, this technique has been extended to measure unknown applied electric fields [62], especially in plasma systems [54, 56, 58–61].

Figure 2 is a simplified schematic for the experimental apparatus for the E-FISH system. Since electric field measurements in a strong plasma was not the primary objective of this work, a femtosecond laser was utilized as the pump source, which allows for measurements of low electric fields at relatively high temporal resolution. The incident laser (hereafter called the pump beam) was generated by amplifying the source light from a Spectra-Physics Mai Tai ultrafast laser through a Spectra-Physics Spitfire Ace regenerative amplifier, which produces a laser with a wavelength of 810 nm, repeating at 1 kHz with FWHM of ~ 80 fs and bandwidth of 20 nm. A half-wave plate (HWP, Thorlabs WPH10M-808) was used to regulate the polarization of the pump beam. Electric field components perpendicular to the pump beam propagation direction can be extrapolated by rotating the polarization of the pump beam with the HWP and measuring the SHG signal at different laser-external electric field couplings.

Before focusing on the PT's distal end, the pump beam is passed through a long pass filter (LP, Thorlabs FEL0450) to remove any SHG signal generated due to the high intensity laser light incident upon the reflective surfaces of upstream optics [61]. The generated SHG signal and residual pump beam were recollimated using an $f = 45$ mm plano-convex lens, and in turn separated through a CaF_2 dispersing prism.

A narrow slit was placed downstream of prism to block the residual pump beam which was not a factor of interest in this work. The SHG signal was reflected by a dichroic mirror (Lattice Electro Optics, WPRs400Tp810) and then focused onto a photomultiplier tube (PMT) powered with a 1000 V DC supply (SRS, PS325). A narrowband pass filter (Thorlabs FB405-10, 405 nm, FWHM 10 nm) was used at the entrance of the PMT to remove stray light. The electric signal from the PMT was recorded by the digital oscilloscope (LeCroy, Model HDO4140A) at the sampling rate of 125 MHz. Aluminum protective screens (Thorlabs TPS5) were placed along the beam path to block any possible interference from the surroundings.

2.3. Phase-locked E-FISH measurements

In general, the voltage gain of a PT cannot be sustained unless the input is dynamically varied in response to changes in the resonant oscillation frequency due to internal heating [12, 69, 70]. However, the input frequency must be fixed to conduct spatiotemporally resolved investigations. Therefore, every electric field presented in this work is the average across 200 successive individual measurements obtained using a phase-locked system. Although the reported values do not capture instantaneous information, they do reflect the average periodic behavior of the electric field induced by the PT.

Both the function generator and the digital oscilloscope were controlled by delay generators (SRS DG645) and synchronized to the pump source. The delay generator divided the trigger signal from the pump source (1 kHz) by 50 times, allowing the PT to be operated in a burst mode with a period of 20 ms. The duty cycle of the burst was set to be 14.9% (~ 3 ms) based on the fact that the number of induced oscillation cycles within a burst (~ 200 cycles) was enough for discharge ignition [13]. During the burst period, SHG signal was acquired at the last input voltage cycle, and signals from 200 successive

bursts were recorded. To map the time evolution of the electric field, one period of the input voltage ($\sim 14.9 \mu\text{s}$) was separated into multiple phases, each with a time interval of 500 ns for the study just below the breakdown threshold and 100 ns for the study slightly above the breakdown threshold, and the PMT was triggered to capture SHG signals for each phase.

The E-FISH method was determined to have a measurement length following the Rayleigh range of the focusing optics [71]. With the optics utilized in this work (Thorlabs, Model LA4306-B, $f = 45 \text{ mm}$), the focused pump beam had a Rayleigh range of $\sim 23 \text{ mm}$ and a width of $75 \mu\text{m}$ in radius. Considering the width of the PT was just 7.5 mm , this large Rayleigh range made localized measurement along the laser propagation direction (y axis as shown in figure 2) infeasible. Consequently, spatially resolved measurements were only conducted by moving the PT and its mounting apparatus along x and z directions. This translation was controlled by a motorized linear stage (Newport, Model M-VP-25XA-XYZR), and the spatial interval was set to be 0.25 mm such that no overlap occurred. To that end, we could scan the pump beam in a large area around the PT and produce a 2D map showing how the electric field is distributed.

2.4. E-FISH calibration and extrapolation of electric field vectors

To relate the measured SHG signal to the external electric field of interest, a plane-wave approximation is usually utilized:

$$I^{(2\omega)} = AN^2(E_{\text{ext}})^2(I_{\text{pump}})^2, \quad (3)$$

where $I^{(2\omega)}$ is the intensity of the induced SHG signal, A is a calibration constant, E_{ext} is the external electric field to be measured, and I_{pump} is the intensity of the pump beam. Based on equation (3), SHG signal can be simply converted to electric field with the help of an absolute calibration. Figure 3 shows the calibration line for this work. Data was collected by passing the pump beam through a known z -oriented electric field generated in the gap between two parallel plates (25.4 mm long \times 12.7 mm wide) and measuring the SHG signal for each laser shot as the electric field was varied.

While the 3rd order nonlinear susceptibility tensor $\chi_{i,j,k,l}^{(3)}$ in equation (2) has 81 components, there are only two independent, nonzero components in a typical E-FISH measurement: the first corresponding to the pump beam polarized parallel to the electric field and the second corresponding to the pump beam polarized perpendicular to the electric field. These components differ by a factor called the susceptibility ratio R [72], leading to a difference factored by R^2 in the measured SHG signal when rotating the polarization of the pump beam (by 90°) relative to the electric field. The susceptibility ratio was measured to be $R = 2.32$ during system calibration by passing both x - and z -polarized pump beams through the z -orientated calibration field.

The sensitivity of the E-FISH method to the field vector makes it possible to simultaneously measure two components of the electric field, E_x and E_z in this work [73]. Electric field components E_x and E_z can be evaluated by:

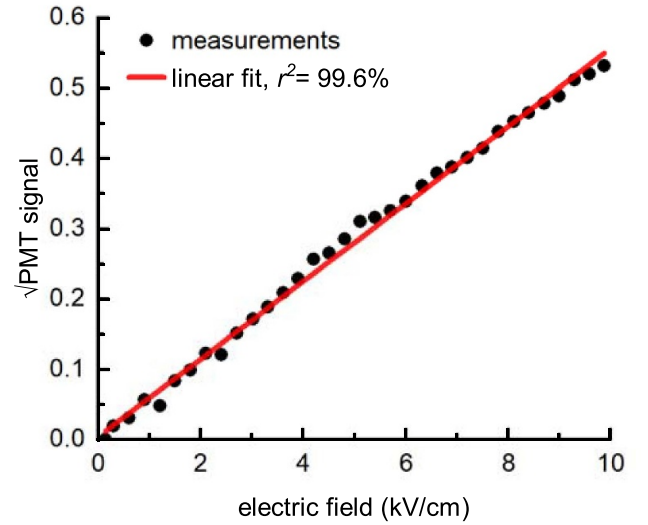


Figure 3. Calibration data (scatter points) taken in 1 atm room air along with the linear best fit line (red line). DC voltages were applied with an increment of 30 V, and the SHG signal (square root of the PMT signal) was measured for the case where the applied laser was polarized parallel to the electric field. Each measurement was an average over 200 successive samples to limit any possible stochasticity.

$$M_{z,\text{pol}} = a + \frac{1}{R}b, \quad (4)$$

$$M_{x,\text{pol}} = b + \frac{1}{R}a, \quad (5)$$

where $M_{z,\text{pol}}$ and $M_{x,\text{pol}}$ are the square root of the PMT signals measured by using z - and x -polarized pump beams, respectively, and R is the measured susceptibility ratio from system calibration. The constants a and b are proportional to $\chi_{z,z,z,z}^{(3)} E_z^{(\text{ext})} E_z^{(\omega)} E_z^{(\omega)}$ and $\chi_{x,x,x,x}^{(3)} E_x^{(\text{ext})} E_x^{(\omega)} E_x^{(\omega)}$ respectively, carrying the information that is only relevant to E_z and E_x .

2.5. Spatially resolved measurements

Spatially resolved measurements were conducted at the phase where the maximum electric field was produced over an entire PT actuation cycle. The input voltage was tuned to a smaller value of $12.5 V_a$ in order to resolve conditions that are just below the breakdown threshold (below-breakdown condition) and a slightly higher value of $14.4 V_a$ to study the electric field just above the breakdown threshold (breakdown condition). The criterion for deciding this threshold for this work was the formation of weak discharge emission that can be observed in the PMT signal along with a small notable feature (small spike) on the sinusoidal input waveform due to the electrical signal induced by the rapid change of the PT's load when a discharge is ignited. The pump beam was scanned over a $4.75 \text{ mm} \times 5.25 \text{ mm}$ region to study the electric field distribution in front of PT's front surface, and over a $4.75 \text{ mm} \times 15.50 \text{ mm}$ region to study the electric field distribution above PT's top surface. Despite the PT's secondary part having a length of 26.5 mm , no measurement was conducted

at more than 15.50 mm from the distal end because of low signal-to-noise ratio (SNR) in this region.

The discussion of the measured electric field distributions is assisted by simulations using COMSOL Multiphysics software with the electrostatics module installed. A 3D COMSOL model of the PT with the same dimension as the secondary part of the PT utilized for the experiments was analyzed, embedding it into a 21 mm long \times 20 mm wide \times 13 mm high rectangular air domain. Extremely fine, physics-control mesh was applied. A ground boundary condition (zero electric potential) was applied to every surface of the air domain except when in contact with the PT model, where a zero-charge boundary condition was utilized. Electric potential boundary conditions were also applied to each surface of the PT model, which is discussed in more detail in section 3.2.

3. Results and discussion

3.1. Electric field distributions around PT's output distal end

Figures 4(a) and (b) show the distributions of the x - and z -components of the electric field ($|E_x|$ and $|E_z|$) over the top surface of the PT operating at the below-breakdown condition. The origin (0, 0) is defined at the center of the PT's front surface, the x axis is along the PT's longitudinal direction, and the z axis is along the PT's transverse direction. Generally, as illustrated in figure 4(a), the value of $|E_x|$ is very small anywhere over the PT's top surface, whereas large values of $|E_z|$, peaking at 20.9 kV cm⁻¹, are observed in the region close to the PT's front corner ($x \sim 0$ –7 mm), as shown in figure 4(b). This strong $|E_z|$ region is due to a geometric effect, which leads to a high electrical potential gradient in the vertical direction and thus enhances the local electric field. The discrepancy in $|E_x|$ and $|E_z|$ indicates that the electric field along the PT's top surface is dominated by the orthogonal z -component.

Figure 5 shows the electric field distribution in front of the PT's distal surface. In contrast to the top surface, a large $|E_x|$ has been measured on the front surface, peaking at 30.3 kV cm⁻¹, as shown in figure 5(a), which is consistent with the expected breakdown field for atmospheric air (roughly 30 kV cm⁻¹ [74]). Likewise, $|E_z|$ is weaker but still reaches ~ 15 –20 kV cm⁻¹ near the top and bottom corners, as shown in figure 5(b). There is a strong $|E_x|$ region (≥ 25 kV cm⁻¹) just next to the front surface, with a steep gradient (70% decrease) extending roughly 3 mm from the surface, and there are lobe-shaped contours that are roughly symmetric around the centerline of the PT. Interestingly, between the lobe-shaped contours there is also a moderately strong region of $|E_x|$ (~ 20 –25 kV cm⁻¹). This phenomenon is due to the nature of the measurement technique. E-FISH is a spatially integrating approach that collects information of the electric field originating from the focal region of the pump beam [71]. When passing the pump beam across the front surface of the PT's distal end, the SHG signal was induced by the strong electric field surrounding the z -oriented edges and integrated into the PMT's output, which in turn leads to the strong electric field region between the lobes. Another interesting aspect of this lobed feature is that the peak field is shifted from the corners.

This is somewhat surprising, as we would expect the field to peak at the corners themselves due to their sharp geometry, where the potential field, in theory, becomes a singularity. We attribute this unanticipated observation to the gradient of the surface potential near the edges of the PT's distal end and will discuss more in the following section.

3.2. Electrical potential distribution on PT's secondary part

As illustrated in figures 4 and 5, there is only one dominant electric field component in each scanning region—the top (E_z) or the front of the distal end (E_x). Therefore, it is possible to evaluate the potential distribution on a specific PT surface by integrating the corresponding dominant electric field relative to a known ground plane (0 V). To do so, we introduced a 50.8 mm long \times 25.4 mm wide grounded horizontal aluminum plate 5 mm ($z = 6.3$ mm) above the PT's top surface for investigations of the top surface potential (V_{top}), and a grounded vertical aluminum plate 5 mm away from the front surface ($x = -5$ mm) for investigations of the potential distribution on the front surface (V_{front}), as shown in the lower left portion of figure 2. Spatially resolved E-FISH measurements were conducted similarly as in section 3.1, and potential values were then evaluated using the following expressions:

$$V_{\text{top}}(x) = \int_{1.3}^{6.3} E_z(x, z) dz \approx \sum_{i=1}^{\frac{h}{\Delta z}} E_{z,i}(x) \cdot \Delta z, \quad (6)$$

$$V_{\text{front}}(z) = \int_0^{-5} E_x(x, z) dx \approx \sum_{i=1}^{\frac{l}{\Delta x}} E_{x,i}(z) \cdot \Delta x, \quad (7)$$

where Δz and Δx are spatial intervals of two adjacent E-FISH measurements along the z and x directions respectively.

The calculated surface potential distribution is shown in figure 6(a) for the top surface. Notably, the potential variation is non-monotonic along the top surface leading away from the front of the PT at $x = 0$ mm, with V_{top} initially increasing, peaking at $x = 1.50$ mm with a value of 5.27 ± 0.28 kV, and then decaying relatively linearly with longitudinal position from $x = 1.50$ mm to 15.50 mm. This linear relation is also reflected in the $|E_x|$ values measured right at the top surface in figure 4(a), which stay almost constant along the longitudinal position, with any deviations mainly due to experimental noise. The offset of the peak in the surface potential near the front surface has also been observed in other experimental explorations using other techniques [37, 42]. We note, however, that analytical modeling [31, 37] suggests that a sinusoidal surface potential distribution is expected on the top surface of the PT that is proportional to the vibrational displacement [11]. This discrepancy between our measurements and model predictions may be possibly due the assumption of neglecting the non-dominant electric field components during integration in equation (6) or that the analytical models in [31, 37] simplify the electromechanical coupling using a 1D analysis, thus not capturing some of the more complex 3D phenomena that occur during actual operation. Spatially resolved

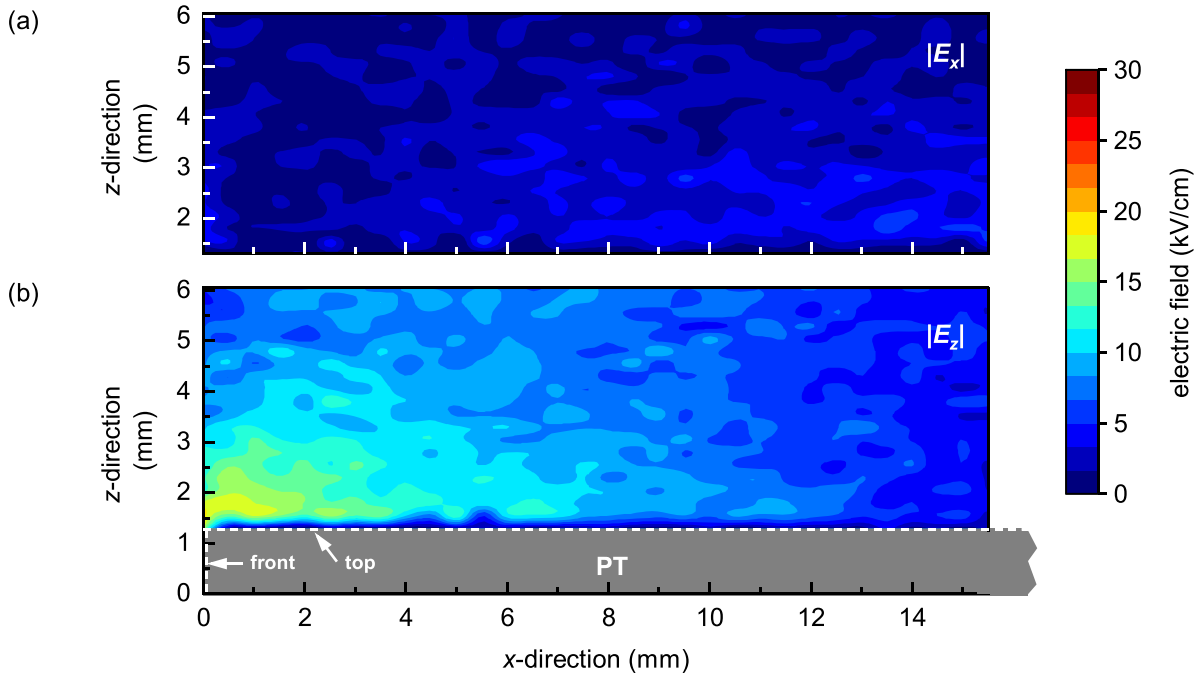


Figure 4. Calibrated contour plots showing the spatial distribution of (a) the x-component $|E_x|$ and (b) the z-component $|E_z|$ of the electric field over the PT's top surface. The origin (0, 0) is defined as the center of the PT's front surface, and the top surface is at $z = 1.30$ mm as illustrated by the white dashed line between the gray region (PT) and the contour plot in (b).

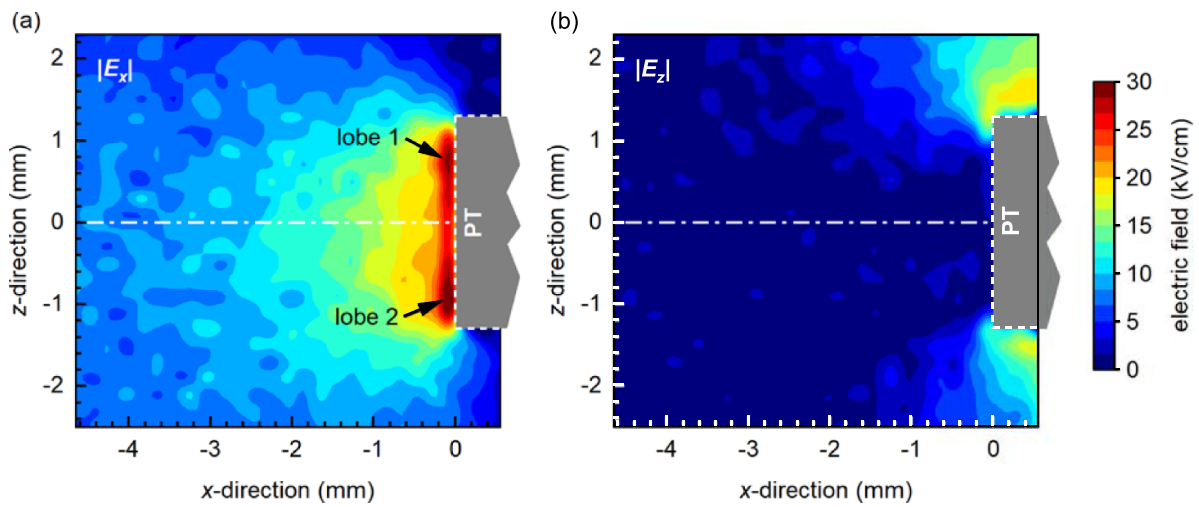


Figure 5. Calibrated contour plots showing the spatial distribution of (a) the horizontal component $|E_x|$ and (b) the vertical component $|E_z|$ of the electric field in front of the PT's distal surface. Two lobed features are denoted with the black arrows.

E-FISH measurements of different PTs (additional materials and/or geometries) would help assess the universal behavior of the measured potential field and the accuracy of the model.

Similar phenomenon is also present in the plot for V_{front} in figure 6(b), where the potential initially increases nearly 1.0 kV from the edges (denoted by the black dashed lines) and then plateaus at a relatively constant value of 5.96 ± 0.16 kV across the front surface. Because of this voltage gradient near the edges, a high electric field appears that is slightly shifted from the top and bottom corners to the middle, resulting in the lobed features shown in figure 5(a) also being shifted from the corners.

To confirm that the potential distribution does in fact lead to the lobed features in $|E_x|$, we conducted 3D COMSOL Multiphysics simulations. Here, the applied electric potential boundary conditions on the PT were consistent with the measured potentials at the PT surface; i.e. they varied non-monotonically on the top surface of the PT in the manner shown in figure 6(a) and took the shape shown in figure 6(b) on the front surface. This potential distribution did in fact lead to two lobed features that are offset from the corners of the PT, as shown in figure 7, consistent with the measurements shown in figure 5(a). To confirm that the potential distribution and electric field are self-consistent, we conducted a number of

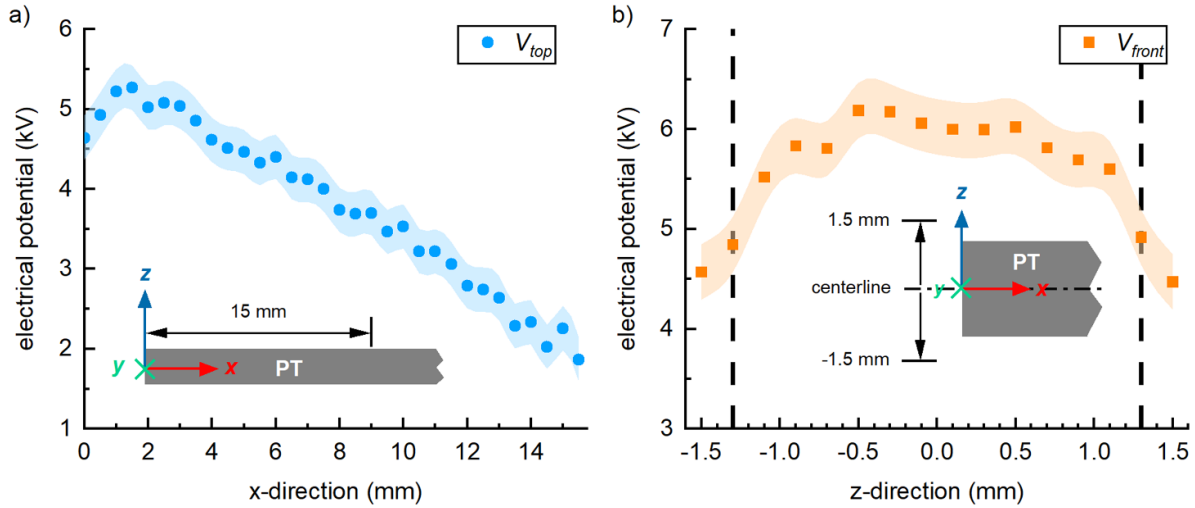


Figure 6. Calculated surface potential distributions on (a) the top surface and (b) the front surface. The front edge of the top surface is at $x = 0$ in (a). The centerline of the PT is at $z = 0$ in (b), and the black dashed lines represent the top and bottom surfaces of the PT. The shaded areas in the plots represent confidence intervals, calculated using the random error of the electric field measurements at one standard deviation (68% confidence).

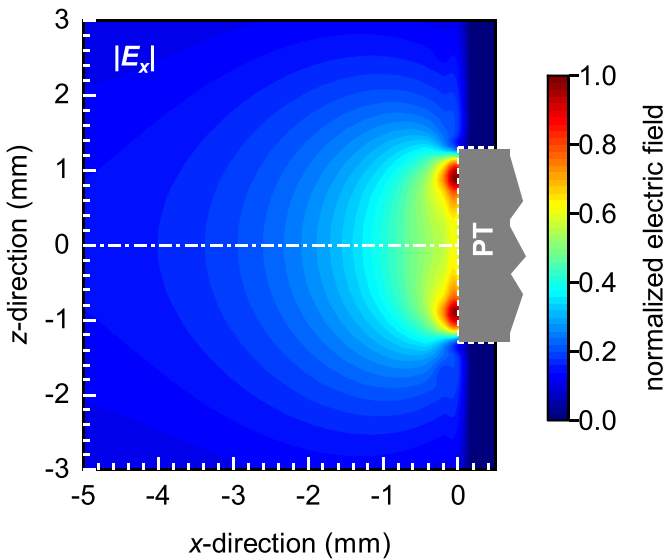


Figure 7. Contour plot of the y-orientated projection of 3D COMSOL simulations of normalized $|E_x|$ showing similar lobed features similar to those in figure 5(a). This lobed behavior was achieved by applying non-monotonic electric potential boundary conditions that were consistent with the measured potentials at the PT surface shown in figure 6.

other simulations with other electric potential boundary conditions on the PT surface, including uniform and linear variations; none of these produced lobed features that were shifted from the top and bottom corners. While these simulations are not predictive, as they are calibrated to the measurements, they do suggest that the unexpected potential variation and lobed electric field are likely real and not measurement artifacts.

As noted earlier, a similar non-monotonic potential distribution on the top surface was measured by Teranishi *et al* [41] using a set of capacitive strip probes. Martin *et al* used 1D analytic modeling to ascribe the non-monotonic behavior to

the effect of an external load in contact with the PT [42], but notably modeling with loads taken into account still overestimated the surface potential near the front surface (although they did improve the accuracy of model predictions at the majority of positions on the PT surface). This reasoning, however, cannot explain the finding in figure 6(b) which shows a relatively uniform voltage distribution with a high value (5.96 ± 0.16 kV) in the middle of the front of the PT with gradients at the edges, instead of a uniform potential on the front surface. Teranishi *et al* themselves ascribed this gradient to the strong electric field's effect on the total capacitance at the divided probes near the front surface used in their measurements [41]. The total capacitance was regarded as constant but found to be smaller in the presence of a strong electric field, leading to an underestimation of the local surface potential. In short, they suggest it was not real, but an artifact of the measurement.

As E-FISH directly measures the electric field without interfering with the operation of the PT or the output load, this potential variation and the ensuing electric field behavior are likely real. An alternative explanation is that the voltage gradient is because of localized depolarization at the edges of the PT crystal induced by ferroelectric behavior. Ferroelectrics are a subset of piezoelectric materials that have a spontaneous polarization that can be switched under the influence of a strong electric field; the PT used in this work was made from PZT, which is also ferroelectric. Geometric enhancement of the electric field surrounding the edges at the PT's distal end is three dimensional and could produce a magnitude higher than the typical coercive field of PZT, which is $\sim 5\text{--}20$ kV cm⁻¹ [75, 76]. Although not measured directly, the locally enhanced fields may cause the PT's non-centrosymmetric unit cells near the edges to switch, potentially offsetting the mechanically induced polarization and in turn leading to a lower surface potential at the edge. Spatially resolved E-FISH measurements starting with lower V_{in} and going to higher V_{in} would help

to prove the presence of ferroelectric behavior if a transition from monotonic distribution to non-monotonic distribution can be observed. Another method for confirming this would be to conduct simulations with ferroelectric phenomenon considered; this could be an interesting direction for future work.

3.3. Temporal evolution of the electric field

To map the temporal evolution of the electric field at the below-breakdown condition, measurements were conducted by separating one period of the input voltage cycle ($\sim 14.9 \mu\text{s}$) into multiple phases with a time interval of 500 ns, with the E-FISH system synchronized to take the data for each of them. The measured temporally resolved SHG signal was related to the electric field using the same DC calibration data discussed above. This approach of using DC calibration data for time-varying E-FISH measurements has been validated in [61]. The PT was again operated with an input voltage of $12.5 V_a$ such that temporally resolved measurements can be compared to the spatially resolved results. Two arrays of data were recorded, the 1st corresponding to the position at $x = -0.50 \text{ mm}$ (slightly off the front surface) and the 2nd corresponding to the position at $x = 0$ (just at the front surface). In each array, there were three z positions measured at 0.25 mm higher than the top surface ($z = 1.55 \text{ mm}$), right at the top surface level ($z = 1.30 \text{ mm}$), and 0.50 mm lower than the top surface ($z = 0.80 \text{ mm}$). Behavior at other locations surrounding the PT were assumed to follow the same distribution as shown in the spatially resolved measurements and thus were not measured here.

Figures 8 and 9 show the temporal evaluation of $|E_x|$ and $|E_z|$, respectively, for data arrays measured at (a) $x = -0.50 \text{ mm}$ and (b) $x = 0 \text{ mm}$. The input voltage was simultaneously recorded while taking temporally resolved E-FISH data and is depicted in panel (c) of each figure. Since the SHG signal scales with the square of electric field, changes in the direction of the electric field components cannot be detected. However, as illustrated in panels (a) and (b) of figures 8 and 9, three successive ‘humps’ (local maxima) can be observed within about one and a half input voltage periods, which indicates that at least one of them belongs to the negative half cycle.

In general, both $|E_x|$ and $|E_z|$ change periodically in time, showing a waveform analogous to a sinusoidal wave with a frequency that is same as the PT’s AC input. The shapes of the three successive peaks are relatively identical when taking the measurement error ($\pm 2.83 \text{ kV cm}^{-1}$) into account, indicating that there is no significant differences between positive and negative half cycles. As shown in figure 8(b), the magnitude of $|E_x|$ measured right at the PT face, $x = 0 \text{ mm}$, is less at the corner of the PT (blue squares) than closer to the centerline of the PT (orange circles) even as the PT cycles, consistent with the lobed feature from the spatially resolved measurements in figure 5(a). As one moves away from the front surface to $x = -0.50 \text{ mm}$, this relationship inverts, and the electric field $|E_x|$ is greater near the corner of the PT (blue squares) and smaller closer to the centerline (orange circles). The electric field measured 0.25 mm above the top surface is much lower by several factors than the field at the face of the PT. As

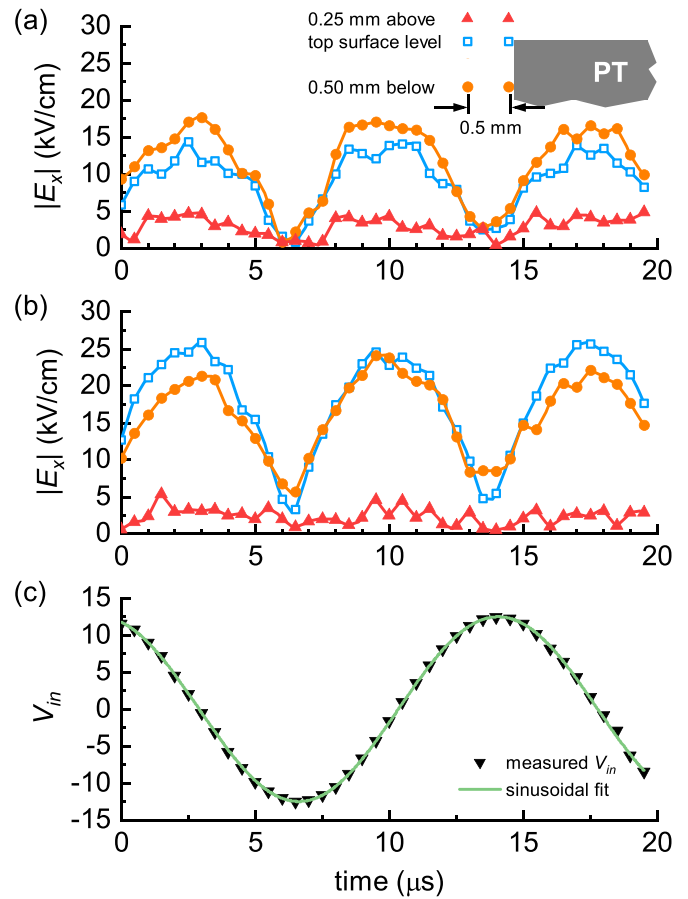


Figure 8. A $20 \mu\text{s}$ excerpt of the temporal evolution of $|E_x|$ for measurements at (a) $x = -0.50 \text{ mm}$ and (b) $x = 0$ (just at the front surface). Each array contains three measurements conducted at 0.25 mm above the top surface (red triangles), top surface level (blue squares), and 0.50 mm below the top surface (orange circles). Each data point has an error of $\pm 2.83 \text{ kV cm}^{-1}$, which is not included on the plots for clarity. Comparison of the PT’s input signal (c) and output signals in (a) and (b) indicates that there is an $\sim 0.45\pi$ delay in phase.

expected, the measured $|E_z|$ was much lower than $|E_x|$ for all positions. Here, the field at the face of the PT was higher at the corner (blue squares) than 0.25 mm above the top surface (red triangles), as shown in figure 9(b), and this also inverts when moving away from the surface to $x = -0.50 \text{ mm}$, illustrated in figure 9(a). These differences in the temporally resolved $|E_x|$ and $|E_z|$ measurements are in good agreement with the spatial distributions shown in the spatially resolved measurements in section 3.1.

The electromechanical coupling in the PT results in a time lag between the input voltage and the induced polarization at the distal end, causing the output voltage and induced electric field to be phase shifted. Figures 8 and 9 clearly show this phase shift in panels (a) and (b) relative to (c). While there is some uncertainty due to the time resolution of the E-FISH measurement and the $\pm 2.83 \text{ kV cm}^{-1}$ uncertainty in the magnitude of the electric field, the phase shift is approximately 0.45π , which is consistent with an estimated $\pi/2$ phase shift as mentioned in [19, 23].

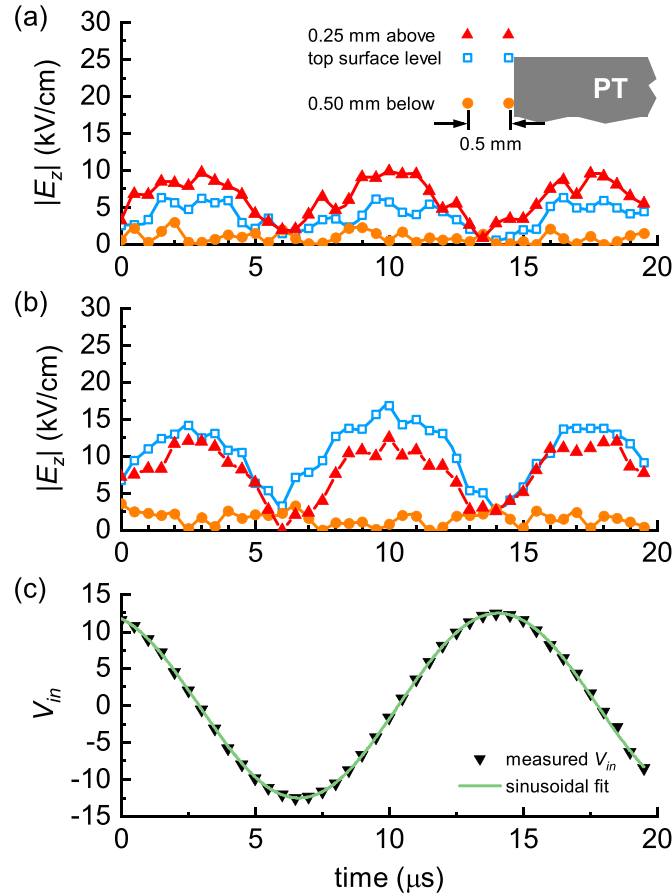


Figure 9. A 20 μs excerpt of the temporal evolution of $|E_z|$ for measurements at (a) $x = -0.5$ mm and (b) $x = 0$ (just at the front surface). Each array contains three measurements conducted at 0.25 mm above the top surface (red triangles), top surface level (blue squares), and 0.50 mm below the top surface (orange circles). Each data point has an error of ± 2.83 kV cm^{-1} , which is not included on the plots for clarity. Comparison of the PT’s input signal (c) and output signals in (a) and (b) indicates that there is an $\sim 0.45\pi$ delay in phase.

3.4. Effects of plasma formation on the electric field

The presence of plasma can cause a decrease in the total impedance of the load at the distal end of the PT as part of the air that acts as a capacitor becomes conductive due to electrical breakdown, which in turn changes the operation of the PT by shifting its resonant frequency and reducing the voltage gain [12, 26, 37, 77]. To study the electric field when plasma is being produced and to understand the possible influence of plasma on the PT’s behavior, 1D temporally resolved E-FISH measurements were conducted at the condition just above the breakdown threshold (breakdown condition). The PT was operated with a slightly higher input voltage of 14.4 V_a , at which weak discharge emissions could be observed in the PMT’s output along with small notable features (small spikes) on the measured sinusoidal input waveform, indicating the presence of a discharge. The pump beam was scanned at the PT’s front surface ($x = 0$) along the z -direction. Ten z positions were measured, from just below the PT’s centerline $z = -0.25$ mm to above the PT top surface $z = 2.25$ mm with a spatial interval of 0.50 mm. E-FISH data was taken every 100 ns at times in the input cycle where discharges were highly likely to be generated [1, 23, 25]. Since the ionization fraction

of this plasma is quite low ($\ll 1\%$) [1, 23, 25], neutral species dominated the plasma. As such, the calibration presented in figure 3 is still valid to relate the measured SHG signal to the electric field despite the presence of radical particles [61].

Figure 10(a) shows contours of the temporal evolution of $|E_x|$ at the breakdown condition, with three z positions measured at 0.50 mm higher than the top surface ($z = 1.80$ mm), right at the top surface level ($z = 1.30$ mm), and 0.50 mm lower than the top surface ($z = 0.80$ mm) plotted in figure 10(b) to show the detailed behavior. As shown in our prior work [25], the plasma formed off of the surface of the PT takes the form of either a single or a multiple ionization wave event occurring during both the positive (forming positive streamers) and negative (forming negative streamers) half-cycles. While streamer formation is consistent, there is appreciable stochasticity when in the cycle they occur, with positive streamers typically generated between 0.8 and 4.8 μs and negative streamers between 8.74 and 12.74 μs in a given cycle. Portions of the input voltage cycle at which E-FISH measurements were conducted are denoted in figure 10(c) for both the positive (left) and negative (right) half cycles.

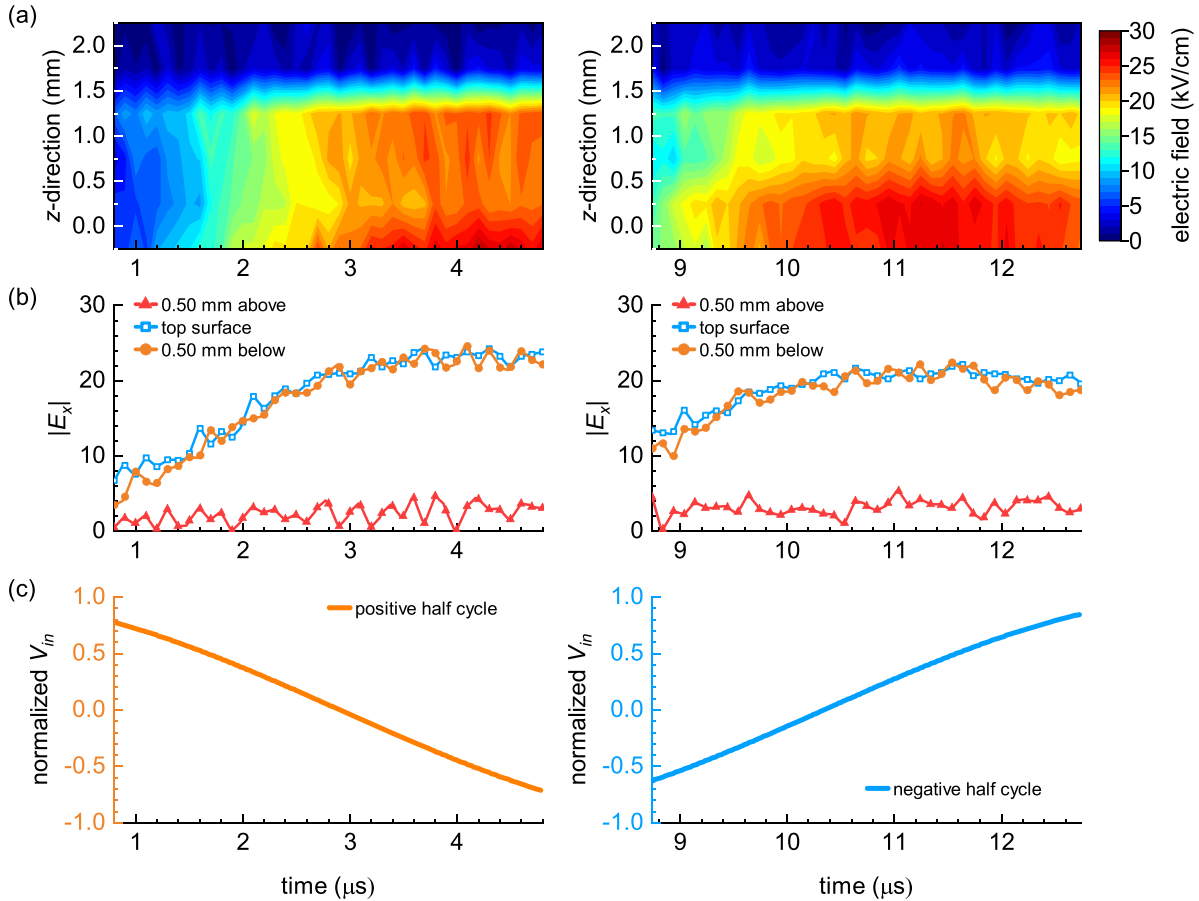


Figure 10. (a) Calibrated contour plots showing the 1D time evolution of $|E_x|$ at the breakdown condition. (b) Temporal evolution of $|E_x|$ measured at three z positions: 0.50 mm above the top surface (red triangles), right at the top surface (blue squares), and 0.50 mm below the top surface (orange circles). Each scatter has an error of $\pm 2.83 \text{ kV cm}^{-1}$, which is not included on the plots for clarity. (c) Portions of the input voltage cycle at which E-FISH measurements were conducted (orange and blue lines). Plots on the left reflect the positive half-cycle and plots on the right reflect the negative half-cycle.

In comparing the below-breakdown (figure 8(b)) and breakdown measurements (figure 10(b)), the electric field magnitudes at breakdown are slightly lower than the below-breakdown condition. Although the charges within the plasma can shield the region surrounding the PT's distal end and theoretically moderate the electric field measured by the E-FISH [61], the density of the charges produced at the condition just above the breakdown threshold, in this work (on the order of 10^{10} cm^{-3}), is far too low to cause an appreciable reduction in the electric field magnitude (likely $\geq 10^{13} \text{ cm}^{-3}$) [1, 25, 78]. We therefore attribute this drop to the reduction of the PT's voltage gain due to the ignition of plasma [12].

Additionally, from figure 10(a) it can be seen that there are several vertical 'stripes' in the contour plots. These 'stripes' coincide with apparent 'kinks' in the scatter plots in figure 10(b) and represent fluctuations in the electric field around the PT's distal end. These fluctuations cannot be correlated to the ionization waves as presented in [59, 61, 79], however, because the temporal resolution of the E-FISH

measurements at the breakdown condition (100 ns) was too low to capture any information of fast propagating ionization waves (on the order of 10^4 to 10^5 m s^{-1}) [61, 79–81]. Hence, they are more likely due to the jitter in the PT's output and/or possibly measurement error. Spectral analysis of these data was also conducted and compared to the measurements at below-breakdown condition, yet yielded no obvious frequency information. Given the limited size of samples available for this analysis (40 temporally resolved samples at one z position), the influence of the plasma's presence on the spectrum at harmonic frequencies, as presented in [12], likely cannot be resolved here. Similar phenomena are also present in the study for $|E_z|$, as shown in figure 11. In general, temporally resolved E-FISH measurements at the breakdown condition only tell limited information. Future E-FISH measurements with higher spatial resolution along the probe beam propagation direction (y direction), sub-nanosecond temporal resolution, and utilizing a picosecond pump source would aid in the exploration of the influence of the plasma on the electric field of PT-based plasma devices.

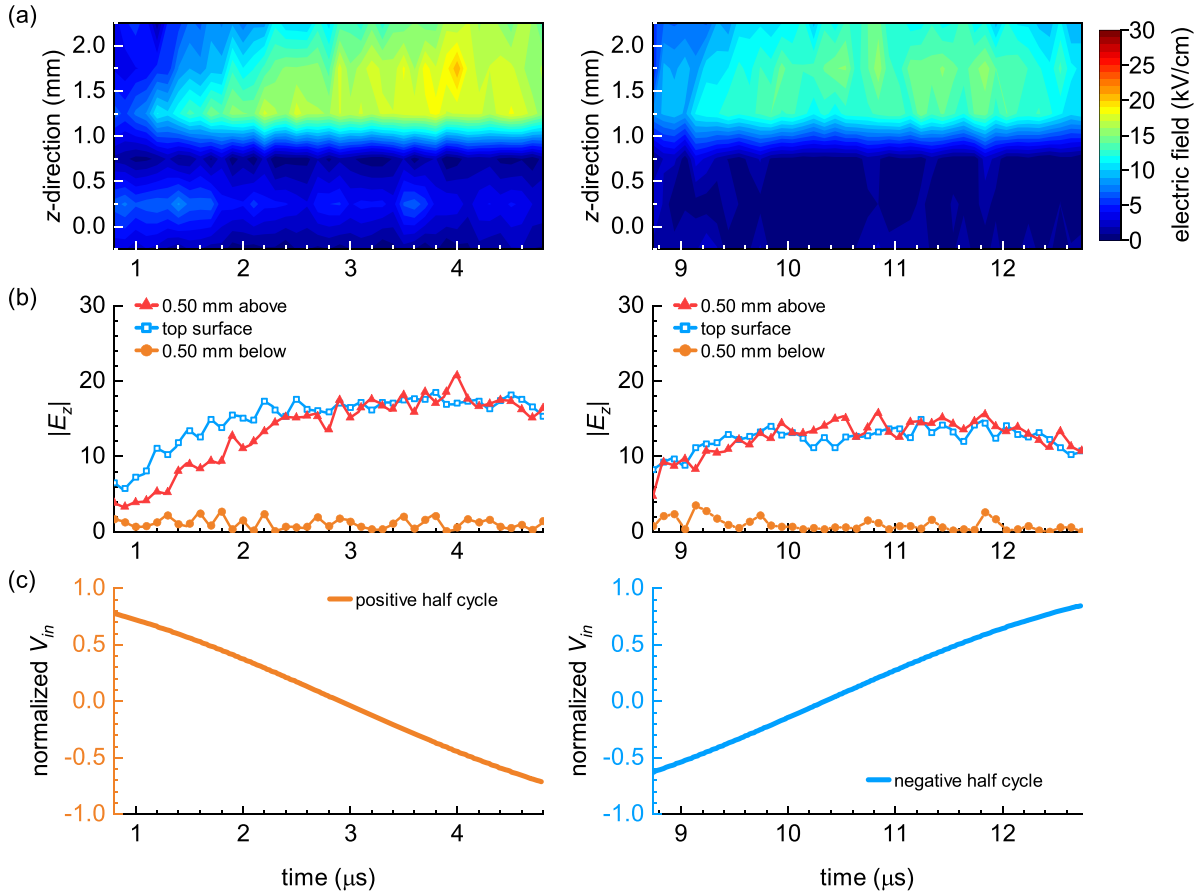


Figure 11. (a) Calibrated contour plots showing the 1D time evolution of $|E_z|$ at the breakdown condition. (b) Temporal evolution of $|E_z|$ measured at three z positions of 0.50 mm above the top surface (red triangles), right at the top surface (blue squares), and 0.50 mm below the top surface (orange circles). Each scatter has an error of $\pm 2.83 \text{ kV cm}^{-1}$, which is not included on the plots for clarity. (c) Portions of the input voltage cycle at which E-FISH measurements were conducted (orange and blue lines). Plots on the left reflect the positive half-cycle and plots on the right reflect the negative half-cycle.

4. Conclusion

Piezoelectric crystals have the potential to be the foundation for mechanical-to-electrical energy conversion plasma sources. Vital to the development of an energy conversion plasma source is establishing a better understanding about how a piezoelectric device would behave when it is used for plasma formation. In this paper, a PT was utilized as a model system to study the spatially and temporally resolved characteristics of the electric field generated at and near the surface of a piezoelectric crystal using E-FISH. Measurements were conducted at conditions either just below the breakdown threshold or slightly above the breakdown threshold. At the below-breakdown condition, the strongest electric field appeared at the front surface of the PT’s distal end, sharply decreasing by 70% over 3 mm from the PT and with an unexpected lobing behavior, nearly symmetric about the PT’s centerline. Surface potential distributions were evaluated on the top and front surfaces of the PT based on the electric field measurements and were consistent with the lobing behavior, which may be indicative of possible ferroelectric processes occurring in the crystal itself. In comparison to the below-breakdown condition, the electric field magnitude measured after breakdown

was slightly lower, which can be attributed to the reduction of the PT’s voltage gain when plasma is active. Future studies on the PT’s polarization and the induced electric field, including exploring other PT materials and conducting simulations, will help answer the question of the voltage gradient near the corners of the PT and aid in developing a comprehensive understanding of PTs and their application as plasma sources.

Data availability statement

The data that support the findings of this study are available upon reasonable request from the authors.

Acknowledgments

This work is based on support from the United States Department of Energy under DE-SC0021083 and the United States National Science Foundation under Award No. PHY-1804091. E-FISH experiments were conducted at the Sandia Low-Temperature Plasma Research Facility at Sandia

National Laboratory in the United States through the support of United States Department of Energy/Sandia National Laboratory Grant 2020F0015. Seong-kyun Im is supported by the National Research Foundation of Korea (NRF) grant funded by the Korea government (MSIT) under Award No. NRF-2020R1C1C1006837.

ORCID iDs

Jinyu Yang  <https://orcid.org/0000-0003-4304-2289>

Seong-kyun Im  <https://orcid.org/0000-0002-7449-4336>

David B Go  <https://orcid.org/0000-0001-8948-1442>

References

- [1] Johnson M J and Go D B 2015 Piezoelectric transformers for low-voltage generation of gas discharges and ionic winds in atmospheric air *J. Appl. Phys.* **118** 243304
- [2] Tan Y K, Hoe K Y and Panda S K 2006 Energy harvesting using piezoelectric igniter for self-powered radio frequency (RF) wireless sensors 2006 *IEEE Int. Conf. on Industrial Technology* pp 1711–6
- [3] Janda M, Martišovits V and Machala Z 2011 Transient spark: a dc-driven repetitively pulsed discharge and its control by electric circuit parameters *Plasma Sources Sci. Technol.* **20** 035015
- [4] Jaenicke O K, Hita Martínez F G, Yang J, Im S and Go D B 2020 Hand-generated piezoelectric mechanical-to-electrical energy conversion plasma *Appl. Phys. Lett.* **117** 093901
- [5] Janda M, Machala Z, Niklová A and Martišovits V 2012 The streamer-to-spark transition in a transient spark: a dc-driven nanosecond-pulsed discharge in atmospheric air *Plasma Sources Sci. Technol.* **21** 045006
- [6] Vazquez Carazo A 2016 Piezoelectric transformers: an historical review *Actuators* **5** 12
- [7] Rosen C A 1956 Ceramic transformer and filters *Proc. Electron. Compon. Symp.* pp 205–11
- [8] Hwang L, Yoo J, Jang E, Oh D, Jeong Y, Ahn I and Cho M 2004 Fabrication and characteristics of PDA LCD backlight driving circuits using piezoelectric transformer *Sens. Actuators A* **115** 73–78
- [9] Lo Y, Lin C and Pai K 2006 Design and analysis of a piezoelectric transformer-based half-bridge resonant inverter for CCFL backlight modules 2006 *IEEE Int. Symp. on Industrial Electronics* vol 2 pp 892–6
- [10] Ben-Yaakov S and Peretz M M 2007 Cold cathode fluorescent lamps driven by piezoelectric transformers: stability conditions and thermal effect *IEEE Trans. Power Electron.* **22** 761–8
- [11] Itoh H, Teranishi K and Suzuki S 2006 Discharge plasmas generated by piezoelectric transformers and their applications *Plasma Sources Sci. Technol.* **15** S51–61
- [12] Korzec D, Hoppenthaler F, Burger D, Andres T and Nettesheim S 2020 Atmospheric pressure plasma jet powered by piezoelectric direct discharge *Plasma Process. Polym.* **17** 2000053
- [13] Korzec D, Hoppenthaler F and Nettesheim S 2021 Piezoelectric direct discharge: devices and applications *Plasma* **4** 1–41
- [14] Itoh H, Teranishi K and Suzuki S 2002 Observation of light emissions around a piezoelectric transformer in various gases *IEEE Trans. Plasma Sci.* **30** 124–5
- [15] Teranishi K, Itoh H and Suzuki S 2002 Dynamic behavior of light emissions generated by piezoelectric transformers *IEEE Trans. Plasma Sci.* **30** 122–3
- [16] Itoh H, Suzuki T, Suzuki S and Rusinov I M 2004 Investigation of ozone loss rate influenced by the surface material of a discharge chamber *Ozone Sci. Eng.* **26** 487–97
- [17] Teranishi K, Suzuki S and Itoh H 2004 A novel generation method of dielectric barrier discharge and ozone production using a piezoelectric transformer *Jpn. J. Appl. Phys.* **43** 6733
- [18] Teranishi K, Shimomura N, Suzuki S and Itoh H 2009 Development of dielectric barrier discharge-type ozone generator constructed with piezoelectric transformers: effect of dielectric electrode materials on ozone generation *Plasma Sources Sci. Technol.* **18** 045011
- [19] Teranishi K, Suzuki S and Itoh H 2005 Dielectric barrier discharge generated by piezoelectric transformer in atmospheric pressure *IEEE Trans. Plasma Sci.* **33** 296–7
- [20] Norgard P, Kovaleski S, Brayfield R S and Garner A L 2018 High-pressure helium plasma produced in the local electric fields of a piezoelectric transformer *IEEE Trans. Plasma Sci.* **47** 128–35
- [21] Teschke M 2009 Piezoelectric low voltage atmospheric pressure plasma sources *Contrib. Plasma Phys.* **49** 614–23
- [22] Kim H, Brockhaus A and Engemann J 2009 Atmospheric pressure argon plasma jet using a cylindrical piezoelectric transformer *Appl. Phys. Lett.* **95** 211501
- [23] Johnson M J, Boris D R, Petrova T B and Walton S G 2019 Characterization of a compact, low-cost atmospheric-pressure plasma jet driven by a piezoelectric transformer *IEEE Trans. Plasma Sci.* **47** 434–44
- [24] Babij M, Kowalski Z W, Nitsch K, Silberring J and Gotszalk T 2014 Atmospheric pressure plasma jet with high-voltage power supply based on piezoelectric transformer *Rev. Sci. Instrum.* **85** 054703
- [25] Yang J, Im S-K and Go D B 2020 Time-resolved characterization of a free plasma jet formed off the surface of a piezoelectric crystal *Plasma Sources Sci. Technol.* **29** 045016
- [26] Ishii K, Akimoto N, Tashiro S and Igarashi H 1998 Influence of load resistance on higher harmonic voltages generated in a piezoelectric transformer *Jpn. J. Appl. Phys.* **37** 5330
- [27] VanGordon J A, Kovaleski S D, Norgard P, Gall B B and Dale G E 2014 Measurement of the internal stress and electric field in a resonating piezoelectric transformer for high-voltage applications using the electro-optic and photoelastic effects *Rev. Sci. Instrum.* **85** 023101
- [28] Pigache F and Nadal C 2011 Modeling and identification of rosen-type transformer in nonlinear behavior *IEEE Trans. Ultrason. Ferroelectr. Freq. Control* **58** 2562–70
- [29] Loyau V, Liu Y and Costa F 2009 Analyses of the heat dissipated by losses in a piezoelectric transformer *IEEE Trans. Ultrason. Ferroelectr. Freq. Control* **56** 1745–52
- [30] Nadal C, Pigache F and Lefevre Y 2012 First approach for the modelling of the electric field surrounding a piezoelectric transformer in view of plasma generation *IEEE Trans. Magn.* **48** 423–6
- [31] Nadal C and Pigache F 2009 Multimodal electromechanical model of piezoelectric transformers by Hamilton's principle *IEEE Trans. Ultrason. Ferroelectr. Freq. Control* **56** 2530–43
- [32] Johnson M J and Go D B 2016 Impingement cooling using the ionic wind generated by a low-voltage piezoelectric transformer *Front. Mech. Eng.* **2** 1–11
- [33] Chaichi A et al 2019 Improvement of tribological and biocompatibility properties of orthopedic materials using piezoelectric direct discharge plasma surface modification *ACS Biomater. Sci. Eng.* **5** 2147–59
- [34] Konchekov E M, Glinushkin A P, Kalinitchenko V P, Artem'ev K V, Burmistrov D E, Kozlov V A and Kolik L V 2021 Properties and use of water activated by plasma of piezoelectric direct discharge *Front. Phys.* **8** 77

- [35] Herianto S, Shih M-K, Lin C-M, Hung Y-C, Hsieh C-W, Wu J-S, Chen M-H, Chen H-L and Hou C-Y 2021 The effects of glazing with plasma-activated water generated by a piezoelectric direct discharge plasma system on whiteleg shrimp (*Litopenaeus vannamei*) *LWT* **154** 112547
- [36] Korzec D, Hoppenhaler F, Shestakov A, Burger D, Shapiro A, Andres T, Lerach S and Nettesheim S 2021 Multi-device piezoelectric direct discharge for large area plasma treatment *Plasma* **4** 281–93
- [37] Teranishi K and Itoh H 2005 Absolute measurement of surface potential and discharge power distributions for piezoelectric transformer-based plasma reactor *Jpn. J. Appl. Phys.* **44** 7083
- [38] Stekic J and Pigache F 2018 Effect of external load resistance on Rosen transformer surface electrical potential *Ferroelectrics* **537** 181–90
- [39] Koga I 1963 Radio-frequency vibrations of rectangular AT-cut quartz plates *J. Appl. Phys.* **34** 2357–65
- [40] Teranishi K, Suzuki S and Itoh H 2001 Luminous phenomenon of silent discharge using a piezoelectric transformer *Jpn. J. Appl. Phys.* **40** 5766
- [41] Teranishi K, Shimomura N and Itoh H 2011 Measurement of surface potential and discharge power for PT-based plasma reactor: effect of electrode edges on surface potential profile *30th International Conf. on Phenomena in Ionized Gases (ICPIG 2011)* pp 1–4
- [42] Martin T, Pigache F and Martin S 2013 Measurement of the electric potential distribution on piezoelectric ceramic surface *2013 IEEE 11th Int. Workshop of Electronics, Control, Measurement, Signals and Their Application to Mechatronics* pp 1–5
- [43] Fotis G P, Gonos I F and Stathopoulos I A 2006 Measurement of the electric field radiated by electrostatic discharges *Meas. Sci. Technol.* **17** 1292–8
- [44] Anikin N B, Starikovskaia S M and Starikovskii A Y 2002 Polarity effect of applied pulse voltage on the development of uniform nanosecond gas breakdown *J. Phys. D: Appl. Phys.* **35** 2785–94
- [45] Takashima K, Adamovich I V, Xiong Z, Kushner M J, Starikovskaia S, Czarnetzki U and Luggenhölscher D 2011 Experimental and modeling analysis of fast ionization wave discharge propagation in a rectangular geometry *Phys. Plasmas* **18** 083505
- [46] Waters R T, Rickard T E S and Stark W B 1972 Direct measurement of electric field at line conductors during AC corona *Proc. Inst. Electr. Eng.* **119** 717–23
- [47] Darny T, Pouvesle J-M, Puech V, Douat C, Dozias S and Robert E 2017 Analysis of conductive target influence in plasma jet experiments through helium metastable and electric field measurements *Plasma Sources Sci. Technol.* **26** 045008
- [48] Hidaka K and Fujita H 1982 A new method of electric field measurements in corona discharge using Pockels device *J. Appl. Phys.* **53** 5999–6003
- [49] Zeng R, Zhuang C, Yu Z, Li Z and Geng Y 2011 Electric field step in air gap streamer discharges *Appl. Phys. Lett.* **99** 221503
- [50] Artem'ev K V, Bogachev N N, Gusein-zade N G, Dolmatov T V, Kolik L V, Konchekov E M and Andreev S E 2020 Study of characteristics of the cold atmospheric plasma source based on a piezo transformer *Russ. Phys. J.* **62** 2073–80
- [51] Obradović B M, Ivković S S and Kuraica M M 2008 Spectroscopic measurement of electric field in dielectric barrier discharge in helium *Appl. Phys. Lett.* **92** 191501
- [52] Sretenović G B, Krstić I B, Kovačević V V, Obradović B M and Kuraica M M 2014 Spatio-temporally resolved electric field measurements in helium plasma jet *J. Phys. D: Appl. Phys.* **47** 102001
- [53] Kovačević V V, Sretenović G B, Slikboer E, Guaitella O, Sobota A and Kuraica M M 2018 The effect of liquid target on a nonthermal plasma jet—imaging, electric fields, visualization of gas flow and optical emission spectroscopy *J. Phys. D: Appl. Phys.* **51** 065202
- [54] Cui Y, Zhuang C and Zeng R 2019 Electric field measurements under DC corona discharges in ambient air by electric field induced second harmonic generation *Appl. Phys. Lett.* **115** 244101
- [55] Cui Y, Zhuang C and Zeng R 2020 Electric field measurements in plasma based on electric field induced second harmonic generation (E-FISH) with nanosecond/picosecond laser *2020 IEEE Int. Conf. on High Voltage Engineering and Application (ICHVE)* pp 1–5
- [56] Simeni M S, Baratte E, Zhang C, Frederickson K and Adamovich I V 2018 Electric field measurements in nanosecond pulse discharges in air over liquid water surface *Plasma Sources Sci. Technol.* **27** 015011
- [57] Cui Y, Wang H, Zhuang C, Luo H, Wang X and Zeng R 2020 Electric field measurement in dielectric barrier discharges using electric field induced second harmonic generation in ambient air *IEEE Trans. Dielectr. Electr. Insul.* **27** 2071–7
- [58] Orr K, Tang Y, Simeni M S, van den Bekerom D and Adamovich I V 2020 Measurements of electric field in an atmospheric pressure helium plasma jet by the E-FISH method *Plasma Sources Sci. Technol.* **29** 035019
- [59] Chng T L, Orel I S, Starikovskaia S M and Adamovich I V 2019 Electric field induced second harmonic (E-FISH) generation for characterization of fast ionization wave discharges at moderate and low pressures *Plasma Sources Sci. Technol.* **28** 045004
- [60] Huang B, Zhang C, Adamovich I, Akishev Y and Shao T 2020 Surface ionization wave propagation in the nanosecond pulsed surface dielectric barrier discharge: the influence of dielectric material and pulse repetition rate *Plasma Sources Sci. Technol.* **29** 044001
- [61] Goldberg B M, Chng T L, Dogariu A and Miles R B 2018 Electric field measurements in a near atmospheric pressure nanosecond pulse discharge with picosecond electric field induced second harmonic generation *Appl. Phys. Lett.* **112** 064102
- [62] Dogariu A, Goldberg B M, O'Byrne S and Miles R B 2017 Species-independent femtosecond localized electric field measurement *Phys. Rev. Appl.* **7** 024024
- [63] Warner A W, Onoe M and Coquin G A 1967 Determination of elastic and piezoelectric constants for crystals in class (3m) *J. Acoust. Soc. Am.* **42** 1223–31
- [64] Jordan N M, Lau Y Y, French D M, Gilgenbach R M and Pengvanich P 2007 Electric field and electron orbits near a triple point *J. Appl. Phys.* **102** 033301
- [65] Sitz P and Yaris R 1968 Frequency dependence of the higher susceptibilities *J. Chem. Phys.* **49** 3546–57
- [66] Ward J F and Bigio I J 1975 Molecular second- and third-order polarizabilities from measurements of second-harmonic generation in gases *Phys. Rev. A* **11** 60–66
- [67] Singer K D and Garito A F 1981 Measurements of molecular second order optical susceptibilities using dc induced second harmonic generation *J. Chem. Phys.* **75** 3572–80
- [68] Bosshard C, Knöpfle G, Prêtre P and Günter P 1992 Second-order polarizabilities of nitropyridine derivatives determined with electric-field-induced second-harmonic generation and a solvatochromic method: a comparative study *J. Appl. Phys.* **71** 1594–605
- [69] Ivensky G, Zafrany I and Ben-Yaakov S 2002 Generic operational characteristics of piezoelectric transformers *IEEE Trans. Power Electron.* **17** 1049–57
- [70] Kahalerras M K, Pigache F, Regnier J and Mosser F 2015 Analyses of temperature influence in piezoelectric transformers dedicated to plasma generation *2015 IEEE Int.*

- Workshop of Electronics, Control, Measurement, Signals and Their Application to Mechatronics (ECMSM)* pp 1–5
- [71] Chng T L, Starikovskaia S M and Schanne-Klein M-C 2020 Electric field measurements in plasmas: how focusing strongly distorts the E-FISH signal *Plasma Sources Sci. Technol.* **29** 125002
- [72] Bigio I J and Ward J F 1974 Measurement of the hyperpolarizability ratio $X_{yyyy}(-2\omega; 0, \omega, \omega)/X_{yyxx}(-2\omega; 0, \omega, \omega)$ for the inert gases *Phys. Rev. A* **9** 35–39
- [73] Chng T L, Naphade M, Goldberg B M, Adamovich I V and Starikovskaia S M 2020 Electric field vector measurements via nanosecond electric-field-induced second-harmonic generation *Opt. Lett.* **45** 1942–5
- [74] Rigden J S and Pippard B 1996 *Macmillan Encyclopedia of Physics* (New York: Simon & Schuster Macmillan)
- [75] Zhang S, Lim J B, Lee H J and Shrout T R 2009 Characterization of hard piezoelectric lead-free ceramics *IEEE Trans. Ultrason. Ferroelectr. Freq. Control* **56** 1523–7
- [76] Lente M H, Picinin A, Rino J P and Eiras J A 2004 90° domain wall relaxation and frequency dependence of the coercive field in the ferroelectric switching process *J. Appl. Phys.* **95** 2646–53
- [77] VanGordon J A, Kovaleski S D, Gall B B, Norgard P, Baxter E A, Kim B H, Kwon J W and Dale G E 2012 Effects of capacitive versus resistive loading on high transformation ratio piezoelectric transformers for modular design considerations *2012 IEEE Int. Power Modulator and High Voltage Conf. (IPMHVC)* pp 675–8
- [78] Rumbach P and Go D B 2012 Fundamental properties of field emission-driven direct current microdischarges *J. Appl. Phys.* **112** 103302
- [79] Goldberg B M, Reuter S, Dogariu A and Miles R B 2019 1D time evolving electric field profile measurements with sub-ns resolution using the E-FISH method *Opt. Lett.* **44** 3853–6
- [80] Teschke M, Kedzierski J, Finantu-Dinu E G, Korzec D and Engemann J 2005 High-speed photographs of a dielectric barrier atmospheric pressure plasma jet *IEEE Trans. Plasma Sci.* **33** 310–1
- [81] Lu X and Laroussi M 2006 Dynamics of an atmospheric pressure plasma plume generated by submicrosecond voltage pulses *J. Appl. Phys.* **100** 063302